Material Identification in Presence of Metal for Baggage Screening

Sandamali Devadithya, David Castañón; Boston University; Boston, MA/U.S.A.

Abstract

Dual-energy imaging has emerged as a superior way to recognize materials in X-ray computed tomography. To estimate material properties such as effective atomic number and density, one often generates images in terms of basis functions. This requires decomposition of the dual-energy sinograms into basis sinograms, and subsequently reconstructing the basis images. However, the presence of metal can distort the reconstructed images. In this paper we investigate how photoelectric and Compton basis functions, and synthesized monochromatic basis (SMB) functions behave in the presence of metal and its effect on estimation of effective atomic number and density. Our results indicate that SMB functions, along with edge-preserving total variation regularization, show promise for improved material estimation in the presence of metal. The results are demonstrated using both simulated data as well as data collected from a dual-energy medical CT scanner.

Introduction

Dual-energy computed tomography (CT) has emerged as a superior way of material characterization in non-destructive imaging. In an ideal type of material characterization, we must be able to accurately estimate properties such as effective atomic number and density of all constituent materials [1]. This can be achieved by reconstructing images in terms of dual-basis functions. In order to do basis decomposition we utilize dual-energy CT, where the objects are scanned with two distinct X-ray energy spectra [2].

An advantage of basis decomposition is it reduces beam hardening artifacts [3]. The linear attenuation coefficient (LAC), which characterise the attenuation of the X-ray beam as it travels through the object is energy-dependent. In conventional CT systems the reconstruction assumes a monochromatic X-ray beam which causes beam hardening and other artifacts leading to poor material characterization.

In dual-energy basis decomposition the most common set of basis functions used are photoelectric absorption and Compton scatter basis (PCB) functions [1, 4], which correspond to two of the primary energy-dependent physical processes that lead to the loss of photons from a transmission path; absorption and scattering respectively. However, the presence of metal or other dense materials in the scene can distort the reconstructed images, particularly the photoelectric image, because few of the lower energy

photons reach the detector. The photoelectric absorption rate at lower energies is significantly higher in metal, and thus is difficult to reconstruct the image given the detector measurements. This is a major concern in security imaging applications for luggage screening, where accurate material characterization is important but dense materials are much common.

In [5] the authors proposed to use synthesized monochromatic basis (SMB) functions to estimate material properties that are system independent. These SMB functions could be generated using any two energy-dependent basis functions. The coefficients of the SMB functions align with the linear attenuation coefficients of the materials at the selected monochromatic energies. Their results show consistent estimation of material properties such as electron density and effective atomic number across a range of materials. However, their scenes did not include dense metallic objects which can introduce significant artifacts and interfere with the estimation of material properties.

Over the years many techniques have been proposed for metal artifact correction in the conventional single-energy spectrum setting [6]. However, there has been little work on alleviating metal artifacts for dual-energy imaging with the use of basis decomposition. One approach that had gain attention in the recent years is to exploit the structure similarity between the Compton and photoelectric images. In [7] and [8], the authors proposed different model-based iterative techniques to jointly estimate photoelectric and Compton coefficients, but showed limited success in reducing metal induced artifacts.

In our prior work [9], we proposed a reconstruction technique based on minimizing weighted least squares estimation with edge-preserving total variation (EPTV) regularization. The material edges which are common to both Compton and photoelectric images can be identified using an initial reconstruction of the high-energy image, and the basis images were reconstructed while preserving these edges. The proposed method outperformed the competing iterative reconstruction algorithms in both simulations and in experiments using data from a medical scanner.

In this paper we investigate how different basis functions behave in the presence of metal and their effect on material identification. We compare the common PCB functions and the SMB functions generated from PCB functions. Although the results in [5] suggest that the order of applying decomposition and linear transformation could be reversed, we show that, in the presence of metal, the basis functions behave differently and hence the choice of basis functions used in the decomposition is significant. We use the reconstructed basis coefficient images to estimate the effective atomic number Z_e and the electron density ρ_e for a range of different materials in the presence of metal. We establish that, with any basis functions, the use of EPTV regularization results in better estimates of material properties over the use of TV regu-

larization. For phantoms when metal is not present, the choice of basis function had little effect in the estimation of Z_e and ρ_e, leading to accuracies similar to those reported in [5]. However, in the presence of metal, our results indicate that directly decomposing with SMB functions and reconstructing with EPTV regularization shows promise for better material estimation. They also show a notable increase in the estimation error of material properties, indicating that further compensation for metal artifacts is desirable to reduce this error.

The rest of the paper is organized as follows: we give an overview of dual-energy X-ray image formation, followed by a detailed description of the basis functions used in our work. Next we present our experiments and conclude with a discussion of results and ideas for future work.

Measurement Model

Dual-energy CT systems collect two measurements of the scene acquired with two distinct X-ray spectral distributions. The Beer-Lambert law indicates that the expected photon counts received at detector j can be modelled as

$$I_i(j) = \int I_0 w_i(E) e^{-\int_{L_j} \mu(r,E) dl} dE \quad (1)$$

with $i = 1,2$ denoting the system spectrum index. The rest of the terms are: E is the energy level, r is the spatial location, $\mu(r,E)$ is the linear attenuation coefficient (LAC) at energy E and position r along the X-ray path L_j, $w_i(E)$ is the ith normalized spectrum at energy E which includes the energy-dependent source strength and detector sensitivity, and I_0 is the source intensity.

Note that the actual received counts at detector j are modeled as a Poisson process with the mean given by (1). Often, we use the negative log of the normalized intensity of photon counts as the measurements which are referred to as sinograms. Let $s_i(j)$ denote the ith energy sinogram at detector j, defined as

$$s_i(j) = -\ln\left(\frac{Z_i(j)}{Z_{i,0}(j)}\right) \quad (2)$$

where $Z_i(j)$ are the actual received counts and $Z_{i,0}(j)$ are the expected photon counts from a direct path with no attenuation on projection L_j.

Having captured two distinct measurements, one can estimate LAC values at two different average energies, which would provide a better characterization of the energy-dependent material properties compared to the estimations acquired from single-energy CT systems. However, the reconstructed individual average attenuation images still suffer from significant artifacts due to the monochromatic approximations and the high attenuation caused by the presence of dense materials. A common approach to alleviate these artifacts is to decompose the dual energy sinograms into basis sinograms, and subsequently reconstruct the decomposed images.

In dual-energy basis decomposition, the energy-dependent LAC of a material is approximated in terms of two energy-dependent basis functions $f_1(E)$ and $f_2(E)$ as

$$\mu(r,E) = x_1(r)f_1(E) + x_2(r)f_2(E) \quad (3)$$

where $x_1(r)$ and $x_2(r)$ are the respective basis coefficients of the material at spatial location r.
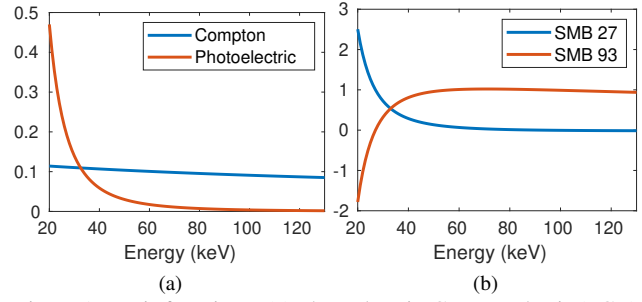

Figure 1: Basis functions: (a) Photoelectric-Compton basis (PCB), (b) Synthesized monochromatic basis (SMB)

Using the basis decomposition in (3), the expected value of normalized counts in (1) can be written as

$$I_i(j) = \int w_i(E) e^{-\int_{L_j}(x_1(r)f_1(E) + x_2(r)f_2(E))dl} dE \quad (4)$$

which can be further simplified as

$$I_i(j) = \int w_i(E) e^{-y_1(j)f_1(E) - y_2(j)f_2(E)} dE \quad (5)$$

where $y_1(j) = \int_{L_j} x_1(r) dl$ and $y_2(j) = \int_{L_j} x_2(r) dl$ are the decomposed basis sinograms. The first step in dual-energy basis image reconstruction is to decompose the high and low energy sinograms $s_1(j), s_2(j)$ into these basis sinograms. We do this using a nonlinear least squares minimization, where we minimize

$$\min_{y_1, y_2} \sum_{i=1}^{2} Z_i(j)(s_i(j) + \ln \int w_i(E) e^{-y_1 f_1(E) - y_2 f_2(E)} dE)^2 \quad (6)$$

Once the sinograms are found, respective coefficients can be modelled as

$$\mathbf{y_1} = \mathbf{A}\mathbf{x_1} \quad \text{and} \quad \mathbf{y_2} = \mathbf{A}\mathbf{x_2} \quad (7)$$

using the forward projection matrix $\mathbf{A}$.

Photoelectric-Compton Basis

The most common basis functions are the photoelectric and Compton functions corresponding to two of the primary energy-dependent physical processes that lead to the loss of photons on the path from source to detector, namely photoelectric absorption and Compton scattering. The Compton scatter basis function is selected as the Klein-Nishina approximation [2] as

$$f_c(\alpha) = \frac{1+\alpha}{\alpha^2}\left(\frac{2(1+\alpha)}{1+2\alpha} - \frac{1}{\alpha}\ln(1+2\alpha)\right) + \frac{1}{2\alpha}\ln(1+2\alpha) - \frac{1+3\alpha}{(1+2\alpha)^2}$$

and the photoelectric absorption basis function is approximated as

$$f_P(E) = \frac{1}{E^3}.$$

The normalized basis functions are illustrated in Fig. 1a. As seen the basis functions behave very differently across the energy spectra. The photoelectric basis function has higher attenuation values
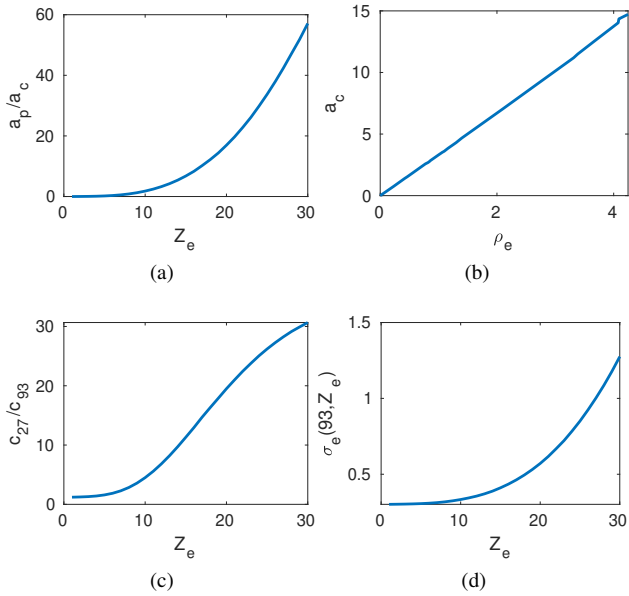
Figure 2: Top row: material estimation from photoelectric-Compton basis, (a) ratio of photoelectric to Compton coefficients vs atomic number, (b) Compton coefficient vs electron density. Bottom row: material estimation from synthesized monochromatic basis, (a) ratio of SMB_{27} to SMB_{93} coefficients vs atomic number, (b) electronic attenuation at 93 keV vs atomic number.

at lower energies while at higher energies the attenuation values are nearly zero. This makes it harder to estimate the photoelectric coefficient when metal is present due to the photon starvation at lower energies.

Once the Compton and photoelectric coefficients are found (a_c and a_p respectively) they can be directly translated into effective atomic number (Z_e) and electron density (ρ_e) [1]. Z_e can be approximated by a function of the ratio of ($\frac{a_p}{a_c}$) and ρ_e is a linear function of a_c. These are depicted in Figs. 2a and 2b for pure elements of atomic number raging from 1 to 30. One can use linear interpolation to estimate Z_e and ρ_e from these curves.

Synthesized Monochromatic Basis

Since the LAC can be approximated by any two energy-dependent basis functions as in (3), at any two energies ,

$$\mu(r, E_L) = x_1(r)f_1(E_L) + x_2(r)f_2(E_L) = c_L(r) \quad (8)$$

$$\mu(r, E_H) = x_1(r)f_1(E_H) + x_2(r)f_2(E_H) = c_H(r) \quad (9)$$

Here c_L and c_H can be defined as the coefficients for the two synthesized monochromatic basis (SMB) functions SMB_L and SMB_H. Using photoelectric and Compton basis functions, the SMB functions can be generated as:

$$\text{SMB}_L(E) = (\frac{f_p(E_H)}{f_c(E_L)f_p(E_H) - f_c(E_H)f_p(E_L)})f_c(E)$$
$$- (\frac{f_c(E_H)}{f_c(E_L)f_p(E_H) - f_c(E_H)f_p(E_L)})f_p(E) \quad (10)$$

$$\text{SMB}_H(E) = (\frac{f_c(E_L)}{f_c(E_L)f_p(E_H) - f_c(E_H)f_p(E_L)})f_p(E)$$
$$- (\frac{f_p(E_L)}{f_c(E_L)f_p(E_H) - f_c(E_H)f_p(E_L)})f_c(E) \quad (11)$$

These are derived in detail in [5].

SMB functions for energies 27 keV and 93 keV are illustrated in Fig. 1b. We chose these energies as they are the most separated energies that are covered by both the spectra of the CT scanner we used. The chosen energies need to be far apart to have a larger contrast in c_L and c_H. As seen they behave similarly across the energy spectra. Furthermore the function values are such that at 27 keV $SMB_{27}(27) = 1$ and $SMB_{93}(27) = 0$, and at 93 keV $SMB_{27}(93) = 0$ and $SMB_{93}(93) = 1$. Note that we have not normalized the SMB functions, in order for this property to hold. Hence these act as monochromatic functions at 27 keV and 93 keV, which has a greater physical significance and can be directly transformed into Z_e and ρ_e. Z_e is a function of the ratio of ($\frac{c_L}{c_H}$) and once Z_e is found ρ_e can be found by,

$$\rho_e = \frac{c_H}{\sigma_e(E_H, Z_e)} \quad (12)$$

Here $\sigma_e(E_H, Z_e)$ is the electronic attenuation at energy E_H. The relationships between Z_e and the ratio ($\frac{c_L}{c_H}$), and between Z_e and $\sigma_e(93, Z_e)$ for pure elements of atomic number ranging from 1 to 30 are depicted in Figs. 2c and 2d. As before one can use linear interpolation to estimate Z_e and ρ_e using these curves.

In [5], the authors suggest that, since SMB is a linear transformation of the root basis, the order of applying decomposition and linear transformation could be reversed. This is in part because of the linear filtered backprojection algorithm used for reconstruction. While this may be appropriate for data with no metal artifacts, these basis functions behave differently in the presence of metal and the choice of basis functions for decomposition matters.

When directly decomposing measurements into SMB sinograms using non-linear least squares as in (6), the Jacobian matrix can end up being singular or having zero values in detectors where there are few counts in the low energy spectrum. This leads to inaccurate material estimation. To avoid this, we use a trust-region algorithm to solve (6) with Steihaug's conjugated gradient method being used to solve the trust-region sub-problem [10]. We vectorized the problem such that a GPU could be utilized for the estimation.

Reconstruction Algorithms

In the presence of metal, conventional CT reconstruction algorithms such as filtered back projection (FBP) would result in significantly distorted images with metal artifacts. Instead, it is preferable to use model-based iterative methods with regularization. One of the most widely used regularization techniques is to minimize weighted least squares with total variation (TV) norm [11]. For any choice of basis function,

$$\hat{\mathbf{x}}_b = \underset{\mathbf{x}_b \geq 0}{\text{argmin}} \frac{1}{2}||\mathbf{y}_b - \mathbf{A}\mathbf{x}_b||^2_{\mathbf{W}_b} + \tau||\mathbf{D}_h\mathbf{x}_b||_1 + \tau||\mathbf{D}_v\mathbf{x}_b||_1 \quad (13)$$

$\mathbf{y}_b$ and $\mathbf{x}_b$ are the basis sinogram and the respective basis coefficients. Here $\mathbf{D}_h$ and $\mathbf{D}_v$ are the horizontal and vertical gradient

operators approximated by the finite differences and $\mathbf{W}_b$ is the weighting matrix. As explained in [9] we approximate $\mathbf{W}_b$ as the inverse covariance of the basis sinogram. τ is the regularization parameter.

However as we showed in [9], TV regularization is not sufficient to alleviate metal artifacts. Hence we proposed a reconstruction algorithm based on minimizing weighted least squares with edge-preserving total variation (EPTV) regularization where we utilized the mutual edges between basis images. We showed that this method surpassed the alternative reconstruction techniques in dual-energy CT with photoelectric-Compton basis decomposition. The idea behind the EPTV regularization is to perform smoothing only on non-edge parts of the image. We accomplished this by penalty weight modifying the TV norm in the regularization. The edges were identified using an initial reconstruction of the high energy image, avoiding errors introduced in the basis sinogram decomposition. The final optimization problem can be modelled as,

$$\hat{\mathbf{x}}_b = \underset{\mathbf{x}_b \geq 0}{\mathrm{argmin}} \frac{1}{2}||\mathbf{y}_b - \mathbf{A}\mathbf{x}_b||_{\mathbf{W}_b}^2 + \tau||\mathbf{W}_h\mathbf{D}_h\mathbf{x}_b||_1 + \tau||\mathbf{W}_v\mathbf{D}_v\mathbf{x}_b||_1$$
(14)

where where $\mathbf{W}_h$ and $\mathbf{W}_v$ are diagonal matrices with weights for horizontal and vertical directions respectively. $\mathbf{W}_h = exp(\frac{-\mathbf{D}_h\mu_{high}}{\beta})$ and $\mathbf{W}_v = exp(\frac{-\mathbf{D}_v\mu_{high}}{\beta})$, where μ_{high} is the high-energy image and β is the controlling parameter.

Problems (13) and (14) are convex but non-differentiable functions and for computational efficacy and numerical stability we chose to use split-Bregman techniques [11] to solve each of the problems. More details on EPTV regularization for dual-energy CT and the implementation steps are described in [9].

Experiments and Results

In this section we present results from simulated data and experimental data based on the the Imatron C300 electron-beam medical scanner. We compare the performance by calculating the relative mean errors for Z_e and ρ_e in three different ways. For the first case we estimate Z_e and ρ_e directly from PCB estimates by interpolating Figs. 2a and 2b. For the second case we estimate the LAC from PCB coefficients and sample the LAC at 27 keV and 93 keV. From the sampled values we estimate Z_e by interpolating Fig. 2c, and ρ_e from (12) for which σ_e can be found by interpolating Fig. 2d. For the final case we estimate Z_e and ρ_e directly from SMB estimates by interpolating Figs. 2c and 2d and substituting to (12). In our experiments we used 95 kVp and 130 kVp spectra (kVp denotes the maximum voltage applied to the X-ray tube). Estimates of the spectra are shown in Fig.3. The reconstructions were carried out with the help of the ASTRA toolbox [12].

Performance Evaluation

Here we present results based on a simulations. We first simulated a 2-D phantom as illustrated in Fig. 4a with different regions corresponding to polypropylene, citric acid, water, sapphire, magnesium, aluminum, black powder, hydrochloric acid, and calcium chloride. These materials were chosen as they spread across a range of effective atomic numbers (Z_e) and electron density (ρ_e) as depicted in Fig. 4b. Next we simulated regions of each material between two copper sheets to investigate how the basis
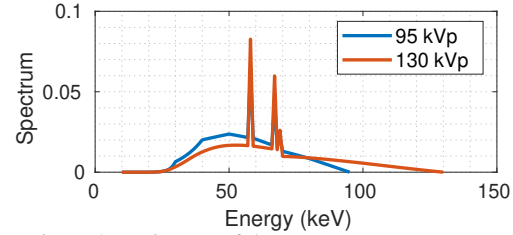
Figure 3: Estimates of the Imatron system spectra
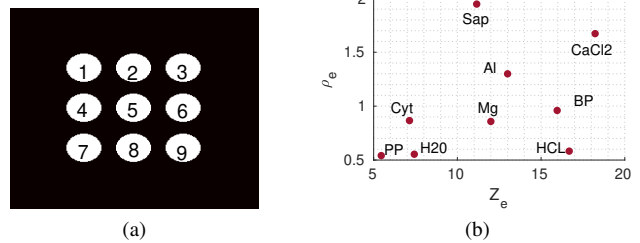
(a)   (b)

Figure 4: 2-D phantom used for in simulations with different materials;(a) 1 - Citric Acid, 2- Hydrochloric Acid, 3-Polypropylene, 4- Aluminium, 5- Water, 6-Calcium Chloride, 7- Black Powder, 8-Sapphire, 9- Magnesium (b) Z_e and ρ_e of the materials
.

functions behave in presence of metal. For both cases Poisson noise was added. For regularization, the parameters that resulted the minimum error were chosen over a range of values.

The geometry of the simulated scanner is such that the parallel sinograms had 180 views over 180 degrees and 512 detector bins at each angle. The reconstructed images are 256x256 with a pixel spacing of 1 mm.

In Fig. 5 reconstruction results for the metal-free phantom are shown. The left two columns show the results with PCB while right two columns shows results with SMB. Reconstructions with both TV and EPTV regularization are shown. With EPTV regularization all the images have got much sharper and in the photoelectric image the streaks around calcium-chloride have been corrected. Table. 1 depicts the averages of relative mean absolute errors for Z_e and ρ_e. It can be clearly seen that with EPTV regularization errors have reduced in both Z_e and ρ_e. Since all the errors are less than 0.5% it is hard to make a claim that one way of estimating Z_e and ρ_e is superior.

Next we investigate the performance when metal is present. We add three balls of each of the materials mentioned above, in between two copper sheets. We do this separately for the materials in order to avoid additional artifacts that arise due to the difference of densities. The reconstruction results for water are shown in Fig. 6 where the left two columns are with PCB and right two

Table 1: Average of relative mean errors across all regions in the metal free phantom

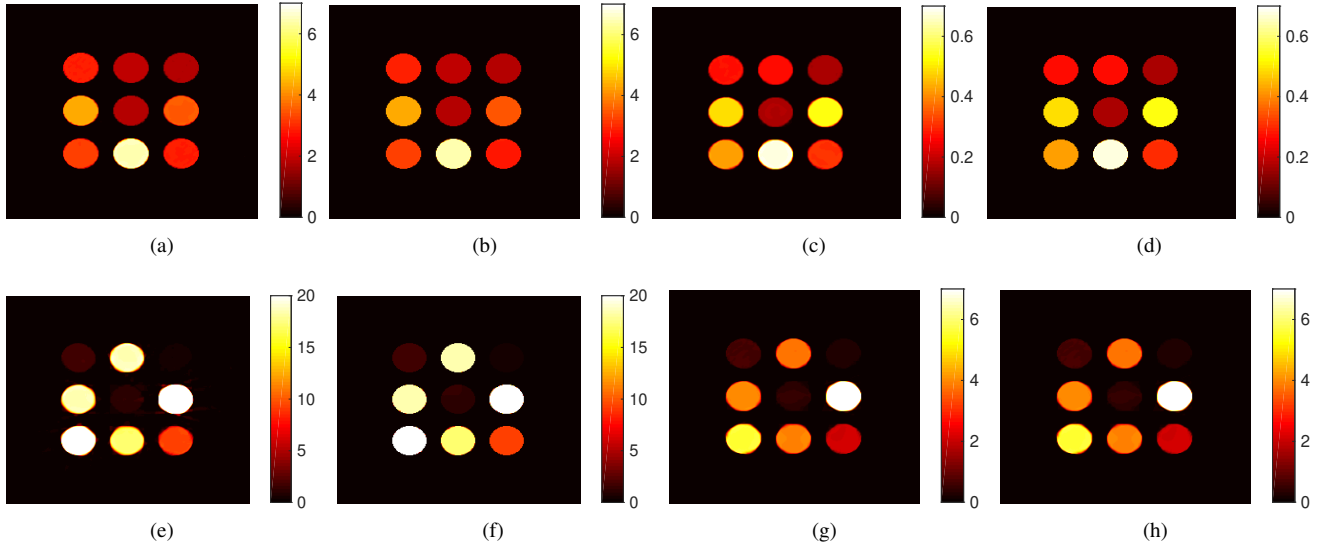| Mean error (%)	Directly from PC		Sampled LAC from PC		Directly from SMB	
	Z_e	ρ_e	Z_e	ρ_e	Z_e	ρ_e
TV	2	0.9	2	0.9	1.9	1
EPTV	0.4	0.5	0.4	0.2	0.4	0.2

Figure 5: Reconstructions for metal-free phantom: The left 2 columns are with PCB and right two columns are with SMB.: (a) Compton with TV, (b) Compton with EPTV, (c) SMB93 with TV, (d) SMB93 with EPTV, (e) photoelectric with TV (f) photoelectric with EPTV, (g) SMB27 with TV, (h) SMB27 with EPTV

Table 2: Average of relative mean errors for all materials in the presence of metal

Mean error (%)	Directly from PC		Sampled LAC from PC		Directly from SMB	
	Z_e	ρ_e	Z_e	ρ_e	Z_e	ρ_e
TV	48.7	2.7	48.7	32.6	40.5	28.8
EPTV	11.8	1	11.7	0.8	5.4	4.8

Table 3: Average of relative mean errors for water region

Mean error (%)	Directly from PC		Sampled LAC from PC		Directly from SMB	
	Z_e	ρ_e	Z_e	ρ_e	Z_e	ρ_e
TV	16.5	10.3	16.5	14	12.6	11.6
EPTV	6.9	11.8	6.9	13	3.1	8.2

columns are with SMB. Reconstructions with both TV and EPTV regularization are shown. The effect of EPTV regularization can clearly be seen in photoelectric and SMB_{27} images for which the images are over-blurred with just TV regularization. Table. 2 depicts the averages of relative mean absolute errors for Z_e and ρ_e across all materials. As seen EPTV regularization have dramatically reduced errors for both Z_e and ρ_e. For estimates of Z_e, estimating directly from SMB is better than estimating from PCB. With EPTV regularization, while the estimates from PCB have an error $\sim 12\%$, estimate from SMB have an error of only $\sim 5\%$. However, when estimating ρ_e the estimates directly from PCB is superior. Even with TV regularization the errors are $\sim 3\%$. The reason for this is because as in Fig. 2b, ρ_e depends only on Compton coefficients and the Compton basis behave very well even in the presence of metal. While the other basis functions have higher attenuation at lower energies, the Compton function does not have a significant affect from the energy values. Hence Compton coefficients do not suffer due to the photon starvation happening at lower energies when metal is present. However, even the estimates from SMB functions have errors around $\sim 5\%$, which may be acceptable, but are significantly higher than the errors when no metal was present.

Another important observation is that the results obtained form sampling the LAC that was estimated using PCB at 27 keV and 93 keV are different from the results obtained with direct de-

composition of SMB. Instead. they are similar to the results estimated directly from PCB coefficients. The only advantage of sampling LAC to estimate Z_e and ρ_e is that the sampled values are system independent as discussed in [5].

To shed additional insight into the results, in Fig. 7 we plot Z_e and ρ_e errors along with basis coefficient errors for each material, when reconstructed with EPTV regularization. For all materials, estimating Z_e directly from SMB gives better results. As seen errors with photoelectric basis are much higher than with SMB_{27} basis and it is reflected in Z_e errors. When analysing individual materials, polypropylene is a material with low density and low atomic number, and sapphire and calcium chloride are high density materials. For these materials, our estimates result in higher Z_e errors. For all materials, estimating ρ_e directly from Compton basis gives better results. As seen errors with Compton basis are better than with SMB_{93} basis and it is reflected in ρ_e errors. Note that ρ_e estimates from SMB basis are less than 5% with the exception of Calcium chloride which is a material with both high density and high effective atomic number.

Experiments with Scanner Data

In this section we present results from experimental data acquired from the Imatron C300 electron-beam medical scanner with the 95 kVp and 130 kVp spectra shown in Fig.3. The re-binned parallel sinograms have 720 angles and 1024 detector bins. Reconstructions of two slices from a bag which contained a wa-
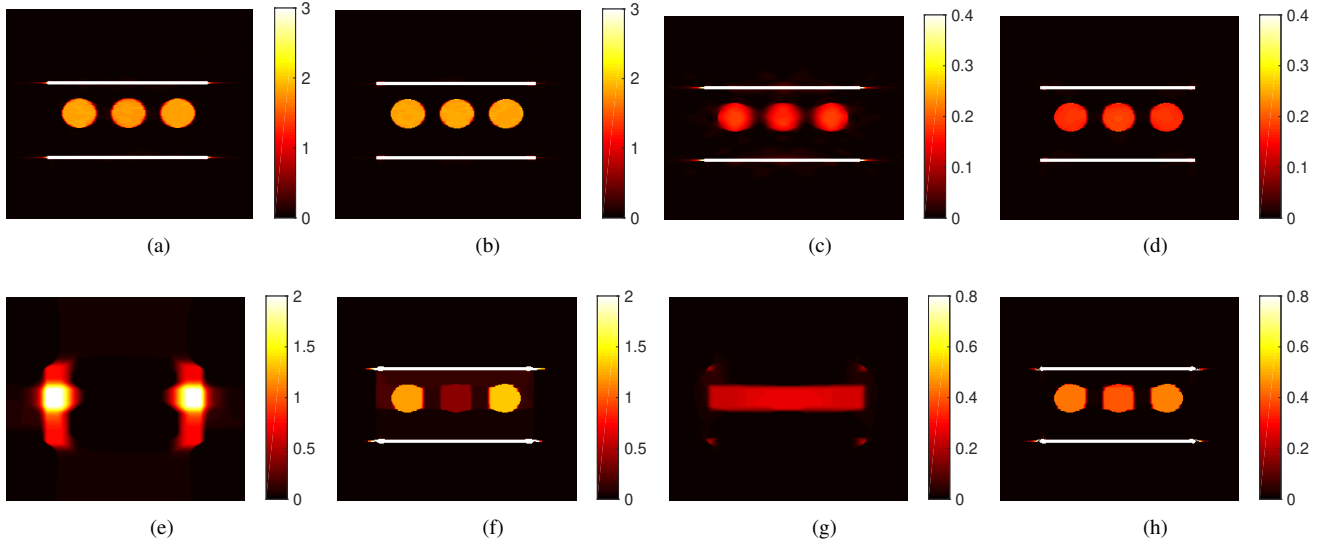
Figure 6: Reconstructions in presence of metal for water balls: The left 2 columns are with PC basis and right two columns are with SMB basis.: (a) Compton with Tv, (b) Compton with EPTV, (c) SMB93 with TV, (d) SMB93 with EPTV, (e) photoelectric with TV (f) photoelectric with EPTV, (g) SMB27 with TV, (h) SMB27 with EPTV
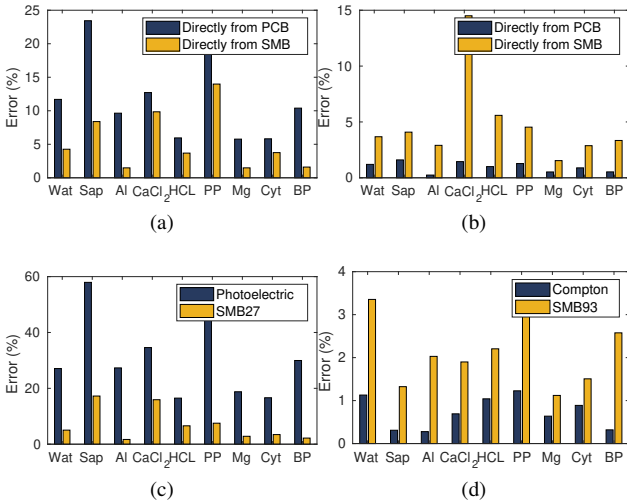

Figure 7: (a) Z_e errors, (b) R_e errors, (c) & (d) basis coefficient errors

.

ter bottle and a rubber sheet with various degrees of metal clutter are presented. The reconstructed images are 512x512 with a pixel spacing of 0.928 mm. The data used here was provided by the ALERT Center of Excellence, and is documented in [13].

In Fig. 8 reconstruction results with EPTV regularization are shown for the two slices. The regularization parameters were chosen empirically. We manually segmented the homogeneous areas of water in both slices and estimated Z_e and ρ_e. Note that we are unable to calculate the errors of rubber as we do not know the exact compounds or the structure of the rubber sheet present. Table 3 depicts the errors with TV and EPTV regularization. For Z_e estimates, SMB gives better results than PCB as in previous cases. For ρ_e estimates, SMB has outperformed PCB. Note that ρ_e errors are around $\sim 10\%$ and are much higher than in previous

simulation cases. This suggests that, while EPTV regularization and SMB are techniques with great potential for estimating material properties in the presence of metal, there is room for improvement.

Discussion

In this paper we investigated how dual-energy reconstructions using different basis functions behave in the presence of metal, and how that affects material characterization. For comparison we estimated Z_e and ρ_e from three different ways; directly from PCB, from sampled LAC estimated using PCB, and directly from SMB. We found that sampling the LAC estimated from a particular basis and then estimating Z_e and ρ_e form those sampled values are similar to that of estimated directly from the original basis coefficients. We initially showed that with any basis functions, the use of EPTV regularization helps in getting better estimates over the use of TV regularization. When metal is not present, the choice of basis function had no significant affect in the estimation of Z_e and ρ_e. In presence of metal, our results indicate that directly decomposing with SMB functions will give a better estimate for Z_e. While estimating ρ_e directly from Compton coefficients turned to be better in our simulation study, estimates from SMB functions were also reasonable. In our experiments with real data the estimates from SMB functions were better than estimates from PCB functions. Hence we can conclude that SMB functions shows promise for better material estimation in presence of metal.

While EPTV regularization and SMB basis appear promising for dual-energy material estimation, the results with metal scatter indicate there is room for improvement. In the future, we will explore combining single-energy sinogram-based metal artifact reduction techniques with the proposed dual-energy reconstruction algorithm. In this work we were limited by the spectra in the CT machine we used. We would like to investigate the behavior of
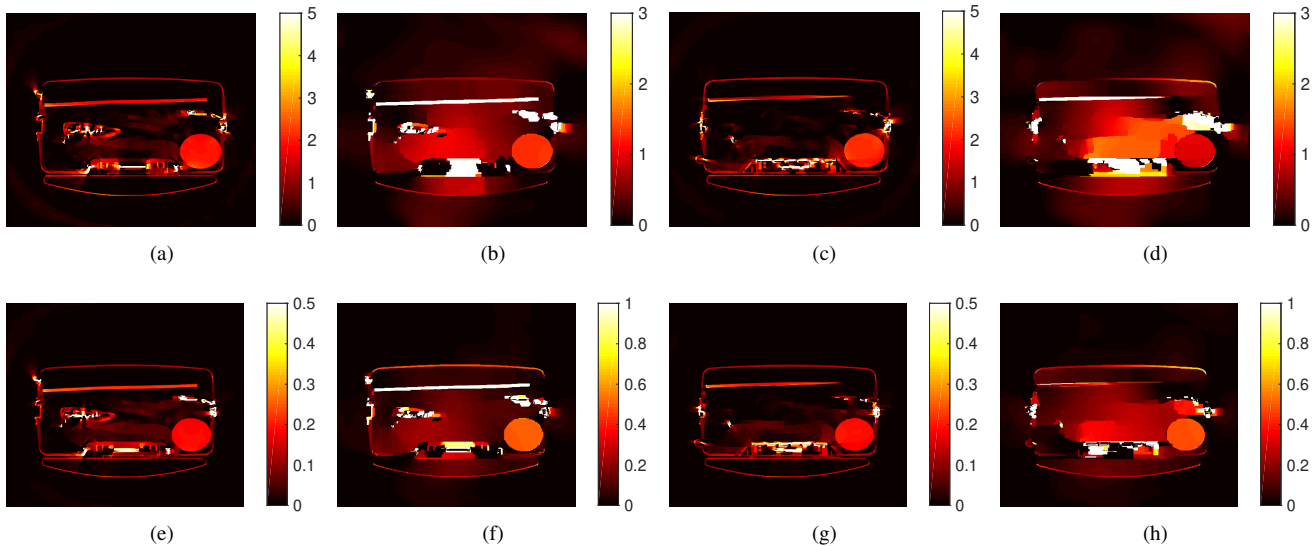
Figure 8: Reconstructions with EPTV norm of slice 1 (columns 1 & 2) and slice 2 (columns 3 & 4): (a) & (c) Compton images, (b) & (d) photoelectric images, (e) & (g) SMB-90 images, (f) & (h) SMB-44 images.

SMB functions at higher energies, with excitation voltages closer to 200 KeV. An important limitation with EPTV regularization is the increased computational complexity over standard iterative reconstruction methods. We will explore approaches for structuring the computations that can reduce this extra computation overhead.

References

[1] S. G. Azevedo, H. E. Martz, M. B. Aufderheide, W. D. Brown, K. M.Champley, J. S. Kallman, G. P. Roberson, D. Schneberk, I. M. Seetho, and J. A. Smith, "System-independent characterization of materials using dual-energy computed tomography," IEEE Transactions on Nuclear Science, vol. 63, no. 1, pp. 341–350, 2016.

[2] R. E. Alvarez and A. Macovski, "Energy-selective reconstructions in X-ray computerised tomography,"Physics in Medicine & Biology, vol. 21, no. 5, p. 733, 1976.

[3] A. C. Kak, M. Slaney, and G. Wang, "Principles of computerized tomographic imaging," Medical Physics, vol. 29, no. 1, pp. 107–107, 2002.

[4] Z. Ying, R. Naidu, and C. R. Crawford, "Dual energy computed tomography for explosive detection," Journal of X-ray Science and Technology, vol. 14, no. 4, pp. 235–256, 2006.

[5] K. M. Champley, S. G. Azevedo, I. M. Seetho, S. M. Glenn, L. D.McMichael, J. A. Smith, J. S. Kallman, W. D. Brown, and H. E. Martz, "Method to extract system-independent material properties from dual-energy X-ray CT," IEEE Transactions on Nuclear Science, vol. 66, no. 3, pp. 674–686, 2019.

[6] L. Gjesteby, B. De Man, Y. Jin, H. Paganetti, J. Verburg, D. Giantsoudi, and G. Wang, "Metal artifact reduction in CT: where are we after four decades?," IEEE Access, vol. 4, pp. 5826–5849, 2016.

[7] B. H. Tracey and E. L. Miller, "Stabilizing dual-energy X-ray computed tomography reconstructions using patch-based regularization," Inverse Problems, vol. 31, no. 10, p. 105–114, 2015.

[8] L. Martin, W. C. Karl, and P. Ishwar, "Structure-preserving dual-energy CT for luggage screening," 2014 IEEE International Conference on Acoustics, Speech and Signal Processing (ICASSP), pp. 1175–1179, 2014.

[9] S. Devadithya and D. Castañón, "Edge-preserving total variation regularization for dual-energy CT images," Electronic Imaging, vol. 2019, no. 13, pp. 147–154, 2019.

[10] T. Steihaug, "The conjugate gradient method and trust regions in larges cale optimization," SIAM Journal on Numerical Analysis, vol. 20, no. 3, pp. 626–637, 1983.

[11] T. Goldstein and S. Osher, "The split Bregman method for L1-regularized problems," SIAM journal on imaging sciences, vol. 2, no. 2, pp. 323–343, 2009.

[12] W. van Aarle, W.J. Palenstijn, J.Cant, E.Janssens, F. Bleichrodt, A. Dabravolski, J.De Beenhouwer, K.J. Batenburg and J.Sijbers, "Fast and flexible X-ray tomography using the ASTRA toolbox", Optics Express, V.24, No.22. 2016.

[13] C. Crawford, H. Martz, and W. C. Karl, "Research and development of reconstruction advances in CT-based object detection systems—Final report," Dept. Homeland Security Center Excellence, ALERT, Boston,MA, USA, Tech. Rep. HSHQDC-12-J-00056, 2013.

Author Biography

Sandamali Devadithya received the B.Sc. in electronics and telecommunication engineering from the University of Moratuwa, Sri Lanka (2013), and the M.S.E.E. from the University of Washington, Seattle, USA (2017). She is currently a Ph.D. candidate at the Department of Electrical and Computer Engineering, Boston University, Boston, USA. Her current research interests include computational imaging and sensing, inverse problems, and digital signal processing.

David Castañón is Professor of Electrical and Computer Engineering at Boston University. He received his Ph.D. in applied mathematics from MIT (1976). He was Chief Scientist at ALPHATECH before joining Boston University (1990). He has been ECE Department Chair, co-director of the Center for Information and Systems Engineering, President of the IEEE Control Systems Society, and member of Air Force's Scientific Advisory Board. His interests include control, estimation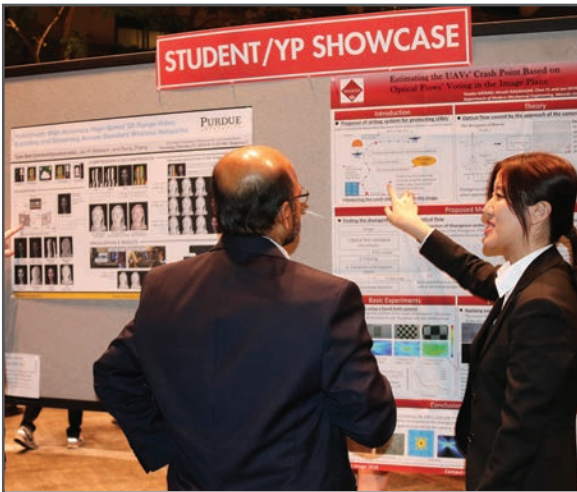, optimization, inverse problems and image understanding.